# Imaging Moving Targets for a Forward Scanning Automotive SAR

# Imaging Moving Targets for a Forward Scanning Automotive SAR

Shahzad Gishkori, David Wright, Liam Daniel, Marina Gashinova and Bernard Mulgrew

***Abstract*—In this paper, we extend the forward-scanning SAR methodology to reconstruct images of the moving targets, for a forward-looking automotive radar. We adapt a matrix decomposition approach to forward-scanning SAR in order to separate moving targets from clutter/stationary objects. To solve our optimisation problem, we propose an iterative solution based on augmented Lagrangian method. Image focusing, over the synthetic aperture, is achieved through spatial segmentation and cross-correlation maximisation. Our proposed method results in well-focused imaging of the moving targets with enhanced angular resolution. Experimental results from simulation as well as real-data corroborate our proposed methodology.**

***Index Terms*—Automotive (forward-looking) SAR, Imaging moving targets, angular resolution, low-rank matrix decomposition.**

## I. Introduction

With the advent of advanced driver assistance systems (ADASs) and highly automated driving (HAD) [1]–[3], automotive radars are increasingly receiving a lot of attention. However, their primary use has been limited to detection only. Imaging an automotive scene has primarily been achieved through optical sensors, e.g., lidar and camera. However, in adverse weather conditions, e.g., rain, fog, snow, etc., imaging capability of the optical sensors is severely hampered. Such conditions are not a limiting factor for the radar. However, imaging with the radar is a very challenging research problem. Recently, some works [4], [5] have appeared, where authors use the automotive radar, operating in low-THz frequency range, as an imaging sensor. One of the major challenges of an automotive radar is to achieve required fine spatial resolution [6], [7], both in range and azimuth. Range resolution can generally be improved by increasing the bandwidth. However, angular (azimuth) resolution (AR) is a function of the radar antenna aperture-size which is limited due to physical constraints and it cannot be increased arbitrarily. A possible way out is to use a synthetic aperture. However, an automotive radar, most of the times, operates in the forward-look direction. This brings in the challenge of AR enhancement for the forward-looking synthetic aperture radar (FL-SAR). A number of previous research papers have looked at the problem of AR enhancement for the FL-SAR for different radar operating environments, e.g., [8]–[14]. Nonetheless, specific to the automotive environment, in [15] we have presented a new approach to AR enhancement for SAR imaging, namely, forward-scanning SAR (FS-SAR). This approach essentially combines scene scanning with SAR processing. There, two back-projection [16] based algorithms, namely, modified back-projection (MBP) algorithm and compressed sensing (CS) [17], [18] based back-projection (CBP) algorithm, generate the SAR image with enhanced AR. The FS-SAR approach has proven to be quite promising and substantial gains can be achieved in automotive SAR imaging. However, [15] assumes stationary targets. In this paper, we extend the FS-SAR approach to imaging moving targets and address the related challenges.

Generally, SAR processing without the consideration of target motion results in defocussing or smearing of the target image, causing a reduction in image resolution [19]. In order to compensate for target motion, a number of methods have been presented in the past, e.g., using the time-frequency signatures [20], matched filtering of the target spectrum [21], image refocusing [22]–[24], back-projection imaging [16], [23]–[26], multi-look imaging schemes [25], [27]–[29], velocity SAR [30], [31] and space-time array processing (with ground moving target indication) schemes [32]–[37]. Most of the previous work is relevant for a side-looking SAR (SL-SAR), instead of FL-SAR. Also, some of these suggested techniques depend on rigorous estimation of target parameters, e.g., range, velocity, trajectory, etc., and some involve specialised processing for target separation from clutter/background. Therefore, the complexity of the SAR image generation/reconstruction, for moving targets, is substantially increased. To circumvent it, in this paper, we seek a non-parametric approach for FS-SAR. In [38], motion compensation is achieved by modelling motion errors as phase errors and then estimating the phase errors in a sparsity-driven framework. This work has been extended in [39] (see also [40] for earlier attempts) where the clutter is separated from the targets by a matrix decomposition approach along with estimating the phase errors. These methods are well modelled for a spotlight mode SAR (Spot-SAR). However, the matrix decomposition approach can still be used to separate clutter from the moving targets for the FS-SAR mode as well, as explained subsequently.

Initially, it was shown in [41] that missing/corrupted entries of a matrix can be recovered under low-rank and incoherence conditions. The idea is similar to recovering sparse signals

S. Gishkori, D. Wright and B. Mulgrew are with Institute for Digital Communications (IDCOM), The School of Engineering, The University of Edinburgh, United Kingdom. Emails: {s.gishkori, d.wright, bernie.mulgrew}@ed.ac.uk

L. Daniel and M. Gashinova are with Microwave Integrated System Laboratory (MISL), School of Electronic, Electrical and Systems Engineering, University of Birmingham, United Kingdom. Emails: {l.y.daniel, m.s.gashinova}@bham.ac.uk

This work was supported by Jaguar Land Rover and the UK-EPSRC grants EP/N012240/1 & EP/N012372/1 as part of the jointly funded Towards Autonomy: Smart and Connected Control (TASCC) Programme.

in CS framework, which have a few large coefficients, low-rank matrices have a few large singular values. Thus, similar to minimising the sum of absolute values of a sparse signal vector (in CS framework), low-rank matrix completion is achieved by minimising the sum of singular values of a matrix [42]. Decomposing a matrix into a low-rank matrix and a sparse matrix, i.e., low-rank plus sparse matrix decomposition (LPSD), was proposed in [43], [44]. The solution basically alternates between estimating the low-rank matrix and the sparse matrix. This approach has been applied in video surveillance, face recognition, background subtraction/movement detection, etc., [44]–[47]. LPSD is particularly useful in dynamic imaging where the low-rank matrix can represent the background, i.e., columns of the low-rank matrix are temporally correlated, and the sparse matrix represents the dynamic part of the image. In our case, the low-rank matrix can represent the clutter and the sparse matrix can represent the moving targets. Thus, an elegant non-parametric method of separating clutter from the moving targets can be achieved.

In this paper, we present a novel imaging technique for FS-SAR mode of an automotive radar. The SAR image measured at each sub-aperture is considered as a temporal snapshot of a target scene. All the temporal snapshots are collected in a matrix. A matrix decomposition approach, LPSD, is applied under the FS-SAR signal model. In order to solve our cost function, we use a state-of-the-art iterative solver, namely, alternating direction method of multipliers (ADMM) [48], [49]. This results in a clutter matrix, containing the stationary targets, and a sparse matrix, containing the dynamic part. Although, the dynamic part has been separated from the clutter, the reconstructed SAR image is still smeared because it is unfocused. Now, image focusing or synthetic-aperture building (in FS-SAR mode) essentially requires tracking the targets over their respective trajectories. In automotive scenarios, these trajectories can assume different geometries and lengths. Thus, motion errors cannot be compensated as merely phase errors. The LPSD process results in a set of temporal snapshots which contain the dynamic-part only and the corresponding reconstructed image shows trajectories of the all the dynamic targets as well. Therefore, we process this set of temporal snapshots and the resulting image, directly, in order to focus the targets. It can be seen that our problem is, primarily, that of segmentation/clustering and association. We need to separate different targets and also build a synthetic aperture. A number of classical methods for segmentation are available in traditional image processing, e.g., K-means, Gaussian mixture, etc., [50]. However, most of these methods are based on pixel value (or intensity). Therefore, patches with the same intensity are categorised as the same clusters. In a radar image, different targets may have the same intensity/reflectivity. Therefore, intensity based segmentation may result in joining multiple targets together. To circumvent this problem, we opt for density-based spatial clustering of applications with noise (DBSCAN) [51]–[53] which is a proximity based clustering scheme. Although, DBSCAN is an effective proximity based method to achieve segmentation, its performance decreases with increasing proximity of the neighboring clusters. Since our aim is to obtain enhanced AR, a straightforward implementation of DBSCAN may prove to be counter-productive. Therefore, we extend DBSCAN to handle the close proximity issues. In order to prove the validity of our proposed method, we provide simulation results of a scenario that emulates the automotive target scene. We have also carried out a measurement campaign to collect real-data in a laboratory-controlled experiment for the same purpose. Results of the experiments verify the effectiveness of our proposed methodology.

***Our Contributions***. The salient contributions of this paper are as given below.

- We extend the FS-SAR methodology, for enhanced AR, to imaging moving targets in an automotive scenario.
- We present a matrix decomposition approach, applicable to FS-SAR mode, in order to separate the dynamic targets from the clutter. In the process, we also obtain the target trajectories.
- To solve our cost function we present an iterative solution based on an augmented Lagrangian method, i.e., ADMM.
- We present an extended DBSCAN methodology for image segmentation/clustering. It has the ability to obtain clusters even in close proximity. Image focusing (or association), over the aperture, is then achieved via cross-correlation maximisation.
- We present experimental results, both with simulation as well as real-data, to verify the validity of our proposed method. We also compare the performance of our proposed method with CBP.

***Organisation***. Section II provides the system model, Section III presents the proposed LPSD method for FS-SAR, Section IV explains the proposed image focusing method, Section V describes step-by-step details of the implementation of the proposed method, Section VI presents experimental results and Section VII provides the conclusions.

***Notations***. Matrices are in upper case bold while column vectors are in lower case bold, $[\mathbf{A}]_{i,j}$ is the $ij$th entry of the matrix $\mathbf{A}$, $\mathbf{I}_N$ is the identity matrix of size $N \times N$, $\mathbf{0}_N$ is a vector of zeros of size $N \times 1$, $(\cdot)^T$ denotes Transpose, $(\cdot)^H$ is Hermitian, $(\cdot)^{-1}$ denotes inverse, $\lfloor \cdot \rfloor$ is the floor function, $\otimes$ stands for the Kronecker product, $\star$ describes the convolution, $\hat{\mathbf{a}}$ is the estimate of $\mathbf{a}$, $\hat{\mathbf{A}}$ is the estimate of $\mathbf{A}$, $\triangleq$ defines an entity, $\uparrow_{\kappa,\kappa'}(\mathbf{A})$ upsamples the matrix $\mathbf{A}$ by an order $\kappa$ along its rows and by an order $\kappa'$ along its columns, the $\ell_p$-norm of a vector $\mathbf{a}$ is denoted as $||\mathbf{a}||_p = (\sum_{i=0}^{N-1} |[\mathbf{a}]_i|^p)^{1/p}$, $\ell_p$-norm of an $M \times N$ matrix is defined as $||\mathbf{A}||_p = (\sum_{i=0}^{M-1}\sum_{i=0}^{N-1} |[\mathbf{A}]_{i,j}|^p)^{1/p}$ and $||\mathbf{A}||_F$ denotes its Frobenius-norm, i.e., $||\mathbf{A}||_{\mathrm{F}} = ||\mathbf{A}||_2$.

## II. System Model

The FS-SAR mode was proposed in [15] to improve the AR in forward-looking automotive radars. It combines scene scanning with SAR processing. At each step over the aperture, the radar scans the target scene (via pulses) at different look-angles and then moves on to the next step over the aperture. Then, the reconstruction algorithm collects information from all scans over the synthetic aperture to generate an image with enhanced spatial resolution. A schematic of the FS-SAR mode

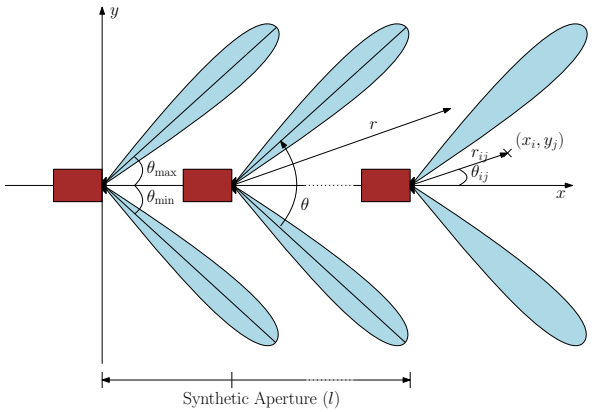


Fig. 1: FS-SAR schematic [15].

can be seen in Figure 1 where the automotive radar scans a target scene at different scan steps, $l = 0, 1, \cdots, L-1$,[1] along the synthetic aperture, with angular range (over the scan), $\theta \in [\theta_{\min}, \theta_{\max}]$ and target range, $r \in (0, R_{\max}]$. In a Cartesian coordinate system, a point is represented as $(x_i, y_j)$ with $x_i$ and $y_j$ being coefficients of $x$-axis and $y$-axis, respectively. Similarly, $r_{ij} \triangleq \sqrt{x_i^2 + y_j^2}$ and $\theta_{ij} \triangleq \arctan(y_j/x_i)$ correspond to equivalent representation in a polar coordinate system. The generic FMCW transmit pulse can be written as

$$s^{\text{Tx}}(t) = \exp\left(j2\pi f_0 t + j\pi\beta t^2\right) \tag{1}$$

where $f_0$ is the carrier frequency, $\beta \triangleq B/T$ is the chirp rate with bandwidth, $B$, and pulse repetition interval (PRI), $T$, and $t : 0 \leq t < T$ is the fast time. The received signal at $l$th scan step and $\theta$th look-angle can be written as

$$s_{l,\theta}(t) = \sum_{u=1}^{U} \alpha_u \exp\left(j2\pi f_0[t - \tau_{l,\theta}(u)] + j\pi\beta[t - \tau_{l,\theta}(u)]^2\right) \tag{2}$$

where $\alpha_u$ is the reflectivity coefficient including the effects of range related variations in the back-scattered energy, $\tau_{l,\theta}(u)$ is the two-way time delay of signal from the $u$th scatterer and $U$ is the total number of scatterers. Note, $U$ can vary for different scans over the aperture. However, for ease of notation, we assume it to be the same. After deramping, low-pass filtering and deskewing [54], (2) can be written as

$$s_{l,\theta}(t) = \sum_{u=1}^{U} \alpha_u \exp(j2\pi(f_0\tau_{l,\theta}(u) + \beta\tau_{l,\theta}(u)t)). \tag{3}$$

The range profile can be obtained as

$$x_{l,\theta}(r) = \mathcal{F}\{s_{l,\theta}(t)\}|_{r=\frac{fc}{2\beta}} \tag{4}$$

where $r$ is the range variable with linear transformation, $r = fc/2\beta$, and $\mathcal{F}\{\cdot\}$ is the Fourier transform operator w.r.t., $t$, corresponding to frequency variable, $f$. The range resolution is defined as, $\Delta_r \triangleq c/2B$, and each range bin is referenced as, $r_{n_r}$, for $n_r = 0, 1, \cdots, N_r - 1$, where $N_r \triangleq R_{\max}/\Delta_r$.

[1]Note, $l$ should refer to physical distance. However, with some abuse of notation, we use it for referencing aperture steps as well.

From (4), the target scene reflectivities along azimuth for the $r_{n_r}$th range bin, i.e., $x_{l,r_{n_r}}(\theta)$, can be given as

$$x_{l,r_{n_r}}(\theta) = \{x_{l,\theta}(r_{n_r})\}_{\theta=\theta_{\min}}^{\theta_{\max}}. \tag{5}$$

Note, we drop the subscript $n_r$ from $x_{l,r_{n_r}}(\theta)$ in the following, to reduce notations. The received signal, along the azimuth, for range $r$ and scan step $l$, can be written as [55],

$$y_{l,r}(\theta) = h(\theta) \star x_{l,r}(\theta) + n_{l,r}(\theta) \tag{6}$$

where $y_{l,r}(\theta)$ is the measured signal, $h(\theta)$ is the antenna beam (assuming the antenna beam-pattern is uniformly sampled over $\theta \in [-\phi, +\phi]$) and $n_{l,r}(\theta)$ is additive white Gaussian noise with variance, $\nu^2$. Let $\delta_\theta = \theta_{3\text{dB}}/\zeta$ represent the fine angular sample/interval, where $\theta_{3\text{dB}}$ is the 3 dB beamwidth and $\zeta$ is a positive integer ($\zeta \geq 1$). Note, a high AR can be modelled by considering $\zeta \gg 1$. Since the radar is not able to take measurements at very fine angular intervals, we define the angular interval for measurements as, $\Delta_\theta = \xi\delta_\theta$, where $\xi \geq 1$. Note, for a very coarse angular measurement interval, $\xi \gg 1$. Let $\mathbf{h} \triangleq [h(-\phi), h(-\phi + \delta_\theta), \cdots, h(+\phi)]^H$ is an $N_h \times 1$ vector, with $N_h = \lfloor 2\phi/\delta_\theta \rfloor + 1$, $\mathbf{y}_{l,r} \triangleq [y_{l,r}(\theta_{\min}), y_{l,r}(\theta_{\min} + \Delta_\theta), \cdots, y_{l,r}(\theta_{\max})]^H$ is an $N_\theta \times 1$ vector, with $N_\theta = \lfloor(\theta_{\max} - \theta_{\min})/\Delta_\theta\rfloor$ and $\mathbf{x}_{l,r} \triangleq [x_{l,r}(\tilde{\theta}_{\min}), x_{l,r}(\tilde{\theta}_{\min} + \delta_\theta), \cdots, x_{l,r}(\tilde{\theta}_{\max})]^H$ is an $N_x \times 1$ vector, with $\tilde{\theta}_{\min} \triangleq \theta_{\min} - (N_h - 1)\delta_\theta/2$, $\tilde{\theta}_{\max} \triangleq \theta_{\max} + (N_h - 1)\delta_\theta/2$ and $N_x = \xi N_\theta + N_h - 1$, where $\tilde{\theta}_{\min}$ and $\tilde{\theta}_{\max}$ ensure that all the targets within the radar beamwidth are accounted for. Similarly, $\mathbf{n}_{l,r} \triangleq [n_{l,r}(\theta_{\min}), n_{l,r}(\theta_{\min} + \Delta_\theta), \cdots, n_{l,r}(\theta_{\max})]^H$ is an $N_\theta \times 1$ vector. Thus, we can write (6) as

$$\mathbf{y}_{l,r} = \mathbf{G}\mathbf{H}\mathbf{x}_{l,r} + \mathbf{n}_{l,r} \tag{7}$$

where $\mathbf{H}$ is the $(\xi N_\theta - 1) \times N_x$ block-Toeplitz matrix, i.e.,

$$\mathbf{H} \triangleq \begin{pmatrix} \mathbf{h}^H & & \mathbf{0}^T_{(N_x - N_h)} \\ 0 & \mathbf{h}^H & \mathbf{0}^T_{(N_x - N_h - 1)} \\ \vdots & \vdots & \vdots \\ \mathbf{0}^T_{(N_x - N_h)} & & \mathbf{h}^H \end{pmatrix} \tag{8}$$

depicting the convolution between antenna beam-pattern and the target reflectivities, and $\mathbf{G}$ is an $N_\theta \times (\xi N_\theta - 1)$ selection matrix, i.e, $[\mathbf{G}]_{n_\theta,:} = [\mathbf{I}_{(\xi N_\theta - 1)}]_{(\xi n_\theta - \xi + 1),:}$, for $n_\theta = 0, 1, \cdots, N_\theta - 1$. Note, we assume $\mathbf{H}$ to be the same for each scan step. However, variations in $\mathbf{H}$ for each scan step can be accommodated in the signal model. We can modify (7) for all range bins as

$$\mathbf{Y}_l = \mathbf{G}\mathbf{H}\mathbf{X}_l + \mathbf{N}_l \tag{9}$$

where $\mathbf{Y}_l \triangleq [\mathbf{y}_{l,0}, \mathbf{y}_{l,\Delta_r}, \cdots, \mathbf{y}_{l,(N_r\Delta_r - N_r)}]$, $\mathbf{X}_l \triangleq [\mathbf{x}_{l,0}, \mathbf{x}_{l,\Delta_r}, \cdots, \mathbf{x}_{l,(N_r\Delta_r - N_r)}]$ and $\mathbf{N}_l \triangleq [\mathbf{n}_{l,0}, \mathbf{n}_{l,\Delta_r}, \cdots, \mathbf{n}_{l,(N_r\Delta_r - N_r)}]$ are $N_\theta \times N_r$, $N_x \times N_r$ and $N_\theta \times N_r$ matrices, respectively.

Note, the system model presented above assumes a stop-and-go principle for the radar. Generally, FMCW pulses are long. Therefore, instantaneous Doppler should be compensated [56]. Since our processing is carried out in the time domain, the approach of [57] can be used in conjunction with our approach to compensate for radar motion during the transmission of FMCW pulses. This

essentially means, shifting the contribution of each pulse by a term which is a function of radar velocity and the squint angle. Nonetheless, for simplicity of presentation, we carry on with the stop-and-go assumption.

## III. LPSD Based FS-SAR Image Decomposition

In this section we develop an LPSD framework for FS-SAR image decomposition. We first explain the basics of LPSD and then present the adaptation of LSPD to FS-SAR.

### A. LPSD Basics

The LPSD aims at decomposing a matrix into a low-rank matrix and a sparse matrix, under certain mild conditions. If $\mathbf{M}$ is a matrix to be decomposed as a superposition of a low-rank matrix, $\mathbf{L}$, and a sparse matrix, $\mathbf{S}$, it can be achieved by solving the following optimisation problem (OP).

$$\min \|\mathbf{L}\|_* + \lambda_e \|\mathbf{S}\|_1 \quad \text{s.t. } \mathbf{M} = \mathbf{L} + \mathbf{S} \tag{10}$$

where $\|\mathbf{L}\|_* \triangleq \sum_k \sigma_k(\mathbf{L})$ is the nuclear norm, i.e, sum of the singular values, $\sigma_k$, of $\mathbf{L}$ and $\lambda_e$ is a positive constant. Note, the nuclear-norm in (10) is an alternative to the explicit rank function, i.e., $\mathrm{rank}(\mathbf{L})$. Minimising a rank function is an NP-hard problem because the rank of a matrix is essentially the total number of non-vanishing singular values of a matrix. In contrast, the nuclear-norm is the sum of the singular values of a matrix and it is a convex function. Raplacing a rank function with a nuclear-norm draws the similar parallels as relaxing an $\ell_0$-norm with an $\ell_1$-norm (in CS framework). Thus, (10) is a (non-smooth) convex OP. Therefore, it can be solved by interior point methods, e.g., CVX [58]. However, for faster, accurate and stable results augmented Lagrangian multiplier methods [59] can also be used.

The decomposition in (10) is unique and an exact recovery of $\mathbf{L}$ and $\mathbf{S}$ is obtained provided the incoherence between these matrices, i.e., the low-rank matrix is not sparse and the sparse matrix is not low-rank. Such incoherence can be achieved if the elements of singular vectors of the low-rank matrix are spread-out (instead of being concentrated and spiky) and non-zero elements of the sparse matrix occur at random locations [44]. Note, the condition of incoherence between the low-rank matrix and the sparse matrix has been inspired by the incoherence notion in CS and draws similar parallels [18], [41].

### B. LPSD for FS-SAR

An FS-SAR image consists of moving targets and stationary objects. Note, we refer to the moving targets as dynamic part of the image and the stationary objects as clutter. Therefore, LPSD can be applied to the FS-SAR mode. However, when the radar is on the move, the dynamic part and the clutter are defined w.r.t. the radar. In order to adapt the LPSD framework to FS-SAR, we assume that imaging concerns a specific area of the target scene and the radar motion has been compensated w.r.t. this specific target area. Therefore, the radar can be considered as if stationary w.r.t. the target area, and the only movement present in the image is due to the moving targets. Note, radar motion can be easily compensated since we already have complete knowledge about it, e.g., via inertial measurement unit (IMU).

Let (9) is written in the following vectorised form.

$$\mathbf{y}_l = \underbrace{[\mathbf{I}_{N_r} \otimes (\mathbf{GH})]}_{\triangleq \mathbf{\Phi}} \mathbf{x}_l + \mathbf{n}_l \tag{11}$$

where $\mathbf{y}_l \triangleq \mathrm{vec}(\mathbf{Y}_l)$, $\mathbf{x}_l \triangleq \mathrm{vec}(\mathbf{X}_l)$ and $\mathbf{n}_l \triangleq \mathrm{vec}(\mathbf{N}_l)$ are $N_\theta N_r \times 1$, $N_x N_r \times 1$ and $N_\theta N_r \times 1$ vectors, respectively, and $\mathbf{\Phi} \triangleq [\mathbf{I}_{N_r} \otimes (\mathbf{GH})]$ is an $N_\theta N_r \times N_x N_r$ joint measurement matrix. Since the aim of FS-SAR is to enhance AR, $N_\theta \ll N_x$. Therefore, (11) is an under-determined system of linear equations. The CBP algorithm in FS-SAR involves solving the following (fused LASSO [60]) OP.

$$\hat{\mathbf{x}}_l = \arg\min_{\mathbf{x}_l} \|\mathbf{y}_l - \mathbf{\Phi}\mathbf{x}_l\|_2^2 + \lambda_e \|\mathbf{x}_l\|_1^1 + \lambda_f \|\mathbf{D}\mathbf{x}_l\|_1^1 \tag{12}$$

where $\lambda_e > 0$ controls element-wise sparsity in $\mathbf{x}_l$, $\lambda_f > 0$ is a fusion penalty parameter and $\mathbf{D}$ is the $N_x N_r \times N_x N_r$ fusion matrix, defined as

$$\mathbf{D} \triangleq \begin{pmatrix} -1 & +1 & 0 & 0 & \cdots & 0 & 0 \\ 0 & -1 & +1 & 0 & \cdots & 0 & 0 \\ \vdots & \vdots & \vdots & \vdots & \vdots & \vdots & \vdots \\ 0 & 0 & 0 & 0 & \cdots & -1 & +1 \\ 0 & 0 & 0 & 0 & \cdots & 0 & +1 \end{pmatrix}. \tag{13}$$

We can see that OP (12) is solved for each aperture position. Then, a composite image can be generated via back-projection. Note, a composite image essentially means, a SAR image, i.e., an image involving all of the aperture samples. Now, in order to adapt the LPSD framework to FS-SAR, we stack the measurements, obtained at each sub-aperture, together and solve the OP, jointly. To this end, we modify (11) in the following form.

$$\mathbf{Y} = \mathbf{\Phi}\mathbf{X} + \mathbf{N} \tag{14}$$

where $\mathbf{Y} \triangleq [\mathbf{y}_0, \mathbf{y}_1, \cdots, \mathbf{y}_{L-1}]$, $\mathbf{X} \triangleq [\mathbf{x}_0, \mathbf{x}_1, \cdots, \mathbf{x}_{L-1}]$ and $\mathbf{N} \triangleq [\mathbf{n}_0, \mathbf{n}_1, \cdots, \mathbf{n}_{L-1}]$ are $N_\theta N_r \times L$, $N_x N_r \times L$ and $N_\theta N_r \times L$ matrices, respectively. Here, our aim is to decompose $\mathbf{X}$ into a low-rank matrix, $\mathbf{C} \triangleq [\mathbf{c}_0, \mathbf{c}_1, \cdots, \mathbf{c}_{L-1}]$, and a sparse matrix, $\mathbf{S} \triangleq [\mathbf{s}_0, \mathbf{s}_1, \cdots, \mathbf{s}_{L-1}]$. Note, the size of $\mathbf{C}$ and the size of $\mathbf{S}$ is the same as the size of $\mathbf{X}$. The low-rank matrix ($\mathbf{C}$) is representative of the clutter or stationary background of the target scene and the sparse matrix ($\mathbf{S}$) is representative of the dynamic part of the target scene, i.e, the moving targets. Now, the LPSD OP for FS-SAR can be written as

$$\begin{aligned} \{\hat{\mathbf{X}}, \hat{\mathbf{C}}, \hat{\mathbf{S}}\} = \arg\min_{\mathbf{X},\mathbf{C},\mathbf{S}} & \frac{1}{2}\|\mathbf{Y} - \mathbf{\Phi}\mathbf{X}\|_F^2 + \lambda\|\mathbf{C}\|_* \\ & + \lambda_e\|\mathbf{S}\|_1^1 + \lambda_f\|\mathbf{D}\mathbf{S}\|_1^1 \\ & \text{s.t. } \mathbf{X} = \mathbf{C} + \mathbf{S} \end{aligned} \tag{15}$$

where $\lambda > 0$ is the penalty parameter for nuclear-norm. A large value of $\lambda$ means a smaller nuclear-norm, i.e., reduced rank of clutter matrix. Solving (15) via ADMM generates the

following OP.

$$\{\hat{\mathbf{X}},\hat{\mathbf{C}},\hat{\mathbf{S}},\hat{\mathbf{Z}},\hat{\mathbf{W}}\} = \underset{\substack{\mathbf{X},\mathbf{C},\mathbf{S}\\ \mathbf{Z},\mathbf{W}}}{\arg\min}\ \frac{1}{2}\|\mathbf{Y}-\mathbf{\Phi X}\|_F^2 + \lambda\|\mathbf{C}\|_* + \lambda_e\|\mathbf{Z}\|_1^1 + \lambda_f\|\mathbf{W}\|_1^1 \quad \text{s.t. } \mathbf{X}=\mathbf{C}+\mathbf{S}, \mathbf{Z}=\mathbf{S}, \mathbf{W}=\mathbf{DS} \tag{16}$$

where $\mathbf{Z}$ and $\mathbf{W}$ are both $N_xN_r \times L$ auxiliary matrices, respectively. An unconstrained form of cost function in (16) can be written as

$$\begin{aligned}\mathcal{L}(\mathbf{X},&\mathbf{C},\mathbf{S},\mathbf{Z},\mathbf{W},\mathbf{K}_X,\mathbf{K}_Z,\mathbf{K}_W)\\ =&\frac{1}{2}\|\mathbf{Y}-\mathbf{\Phi X}\|_F^2 + \lambda\|\mathbf{C}\|_* + \lambda_e\|\mathbf{Z}\|_1^1 + \lambda_f\|\mathbf{W}\|_1^1\\ &+\langle\mathbf{K}_X,(\mathbf{X}-\mathbf{C}-\mathbf{S})\rangle + \frac{\mu_X}{2}\|\mathbf{X}-\mathbf{C}-\mathbf{S}\|_F^2\\ &+\langle\mathbf{K}_Z,(\mathbf{Z}-\mathbf{S})\rangle + \frac{\mu_Z}{2}\|\mathbf{Z}-\mathbf{S}\|_F^2\\ &+\langle\mathbf{K}_W,(\mathbf{W}-\mathbf{DS})\rangle + \frac{\mu_W}{2}\|\mathbf{W}-\mathbf{DS}\|_F^2\end{aligned} \tag{17}$$

where $\mathbf{K}_X$, $\mathbf{K}_Z$ and $\mathbf{K}_W$ are all $N_xN_r \times L$ matrices containing column vectors of Lagrange multipliers, $\langle\mathbf{K},\mathbf{A}\rangle \triangleq \mathrm{tr}(\mathbf{K}^H\mathbf{A})$ is the inner product of two matrices, $\mathrm{tr}(\cdot)$ is a trace operator and $\mu_X, \mu_Z, \mu_W$ are positive constants impacting the rate of convergence. A solution of (16) can be obtained by the following successive approximations.

$$\hat{\mathbf{X}}^{[n]} = \underset{\mathbf{X}}{\arg\min}\,\mathcal{L}\left(\mathbf{X},\mathbf{C}^{[n-1]},\mathbf{S}^{[n-1]},\mathbf{K}_X^{[n-1]}\right) \tag{18}$$

$$\hat{\mathbf{C}}^{[n]} = \underset{\mathbf{C}}{\arg\min}\,\mathcal{L}\left(\mathbf{X}^{[n-1]},\mathbf{C},\mathbf{S}^{[n-1]},\mathbf{K}_X^{[n-1]}\right) \tag{19}$$

$$\hat{\mathbf{S}}^{[n]} = \underset{\mathbf{S}}{\arg\min}\,\mathcal{L}\left(\mathbf{X}^{[n-1]},\mathbf{C}^{[n-1]},\mathbf{S},\mathbf{Z}^{[n-1]},\mathbf{W}^{[n-1]},\mathbf{K}_X^{[n-1]},\mathbf{K}_Z^{[n-1]},\mathbf{K}_W^{[n-1]}\right) \tag{20}$$

$$\hat{\mathbf{Z}}^{[n]} = \underset{\mathbf{Z}}{\arg\min}\,\mathcal{L}\left(\mathbf{S}^{[n-1]},\mathbf{Z},\mathbf{K}_Z^{[n-1]}\right) \tag{21}$$

$$\hat{\mathbf{W}}^{[n]} = \underset{\mathbf{W}}{\arg\min}\,\mathcal{L}\left(\mathbf{S}^{[n-1]},\mathbf{W},\mathbf{K}_W^{[n-1]}\right) \tag{22}$$

which involves differentiating $\mathcal{L}$ w.r.t. the optimisation variable while keeping other variables fixed, at each $n$th iteration, until convergence. Update for Lagrange multipliers is given as

$$\mathbf{K}_X^{[n]} = \mathbf{K}_X^{[n-1]} - \mu_X\left(\mathbf{X}^{[n]}-\mathbf{C}^{[n]}-\mathbf{S}^{[n]}\right) \tag{23}$$

$$\mathbf{K}_Z^{[n]} = \mathbf{K}_Z^{[n-1]} - \mu_Z\left(\mathbf{Z}^{[n]}-\mathbf{S}^{[n]}\right) \tag{24}$$

$$\mathbf{K}_W^{[n]} = \mathbf{K}_W^{[n-1]} - \mu_W\left(\mathbf{W}^{[n]}-\mathbf{DS}^{[n]}\right). \tag{25}$$

Now, solving (18) we get

$$\hat{\mathbf{X}}^{[n]} = \left(\mathbf{\Phi}^H\mathbf{\Phi}+\mu_X\mathbf{I}\right)^{-1} \times\left(\mathbf{\Phi}^H\mathbf{Y}+\mu_X\left(\mathbf{C}^{[n-1]}+\mathbf{S}^{[n-1]}\right)-\mathbf{K}_X^{[n-1]}\right) \tag{26}$$

where the inverse in (26) does not depend on $\mathbf{X}$. Therefore, it can be obtained off-line. Solving (19) we get

$$\mathbf{C}^{[n]} = \chi\left(\left(\mathbf{X}^{[n-1]}-\mathbf{S}^{[n-1]}+\frac{1}{\mu_X}\mathbf{K}_X^{[n-1]}\right),\frac{\lambda}{\mu_X}\right) \tag{27}$$

where $\chi(\cdot,\cdot)$ is a thresholding function of the singular values, defined as

$$\chi\left(\mathbf{A},\lambda\right) = \mathbf{U}\,\eta\left(\mathbf{\Sigma},\lambda\right)\,\mathbf{V}^H \tag{28}$$

where matrices $\mathbf{U}$, $\mathbf{\Sigma}$ and $\mathbf{V}$ are obtained via SVD of $\mathbf{A}$, i.e., $\mathrm{svd}(\mathbf{A}) = \mathbf{U\Sigma V}^H$ and $\eta(\cdot,\cdot)$ is an element-wise thresholding function, defined as

$$\eta\left(s,\lambda\right) = \frac{s}{|s|}\max\left(|s|-\lambda,0\right) \tag{29}$$

where $s$ can be a complex variable. Note, $\eta\left(\mathbf{\Sigma},\lambda\right)$ would apply (29) to each element of $\mathbf{\Sigma}$. Thus, $\chi\left(\mathbf{A},\lambda\right)$ involves doing SVD of $\mathbf{A}$, thresholding the singular values of $\mathbf{A}$ w.r.t. $\lambda$ and then, reconstituting $\mathbf{A}$. Solving (20) we get

$$\begin{aligned}\hat{\mathbf{S}}^{[n]} =& \left(\mu_W\mathbf{D}^H\mathbf{D}+\left(\mu_Z+\mu_X\right)\mathbf{I}\right)^{-1}\\ &\times\Big(\mu_X\left(\mathbf{X}^{[n-1]}-\mathbf{C}^{[n-1]}\right)+\mu_Z\mathbf{Z}^{[n-1]}+\mathbf{K}_X^{[n-1]}\\ &+\mathbf{K}_Z^{[n-1]}+\mathbf{D}^H\mathbf{K}_W^{[n-1]}+\mu_W\mathbf{D}^H\mathbf{W}\Big)\end{aligned} \tag{30}$$

where the inverse component in (30) is independent of $\mathbf{S}$. Therefore, it can also be computed off-line. Solving (21) we get

$$\mathbf{Z}^{[n]} = \eta\left(\left(\mathbf{S}^{[n-1]}-\frac{1}{\mu_Z}\mathbf{K}_Z^{[n-1]}\right),\frac{\lambda_e}{\mu_Z}\right) \tag{31}$$

and solving (22) we get

$$\mathbf{W}^{[n]} = \eta\left(\left(\mathbf{DS}^{[n-1]}-\frac{1}{\mu_W}\mathbf{K}_W^{[n-1]}\right),\frac{\lambda_f}{\mu_W}\right) \tag{32}$$

where $\eta(\cdot,\cdot)$ is defined in (29). The iterations stop once the desired convergence has been achieved. The stopping criterion can be either an update tolerance or the maximum number of iterations. The estimates $\hat{\mathbf{S}}$, $\hat{\mathbf{C}}$ and $\hat{\mathbf{X}}$ can now be used to generate an image of dynamic targets only (i.e., $\gamma^{\hat{\mathbf{S}}}$ for composite and $\gamma^{\hat{\mathbf{s}}_l}$ for $l$th aperture), clutter only (i.e., $\gamma^{\hat{\mathbf{C}}}$ for composite and $\gamma^{\hat{\mathbf{c}}_l}$ for $l$th aperture) and their combination (i.e., $\gamma^{\hat{\mathbf{X}}}$ for composite and $\gamma^{\hat{\mathbf{x}}_l}$ for $l$th aperture), respectively.

## IV. FS-SAR Image Focusing

Although, LPSD separates clutter from the moving targets, the resulting image is still smeared. Therefore, image focusing is required. This focusing is not the same as traditional image focusing. Due to the FS-SAR mode, we need to collect information from each scan step and combine it coherently to build a synthetic aperture. Image focusing, for the FS-SAR images of the moving targets, can be considered here as a synonym for synthetic aperture building. To this end, we turn to image segmentation approaches. We use an extended DBSCAN approach to obtain clustering. Afterwards, we use correlation maximisation to focus moving targets (or build synthetic aperture), as explained in the following.

### A. DBSCAN Basics

Given a set, $\mathcal{P}$, of image pixels, segmentation/clustering procedure partitions it into clusters, $\mathcal{U}_u$, for, $u = 0,\cdots,\breve{U}-1$, based on a distance measure, e.g., Euclidean distance or Manhattan distance, such that, $\bigcup_{u=0}^{\breve{U}-1}\mathcal{U}_u = \mathcal{P}$ and $\bigcap_{u=0}^{\breve{U}-1}\mathcal{U}_u = \emptyset$.

Generally, clustering algorithms consider pixel values (or intensities) as elements in $\mathcal{P}$. However, DBSCAN is a proximity based algorithm and considers spatial proximity of pixels for clustering/segmentation. Therefore, $\mathcal{P}$ consists of Cartesian coordinates of the significant points. There are a few important parameters associated with DBSCAN. In the following, we briefly describe them for the sake of clarity of the proposed methodology. See [51] for more details.

*$\epsilon$-Neighborhood*. In DBSAN, the proximity between two points is established through a distance measure. The Euclidean distance between two points, $a$ at $(x_i, y_j)$ and $b$ at $(x_{i'}, y_{j'})$, can be written as, $\Delta_{ab}^{\text{prox}} = \sqrt{(x_i - x_{i'})^2 + (y_j - y_{j'})^2}$. Now, the $\epsilon$-neighborhood of the point $a$ can be defined as, $\mathcal{N}_a^{\epsilon} \triangleq \{b \in \mathcal{P} : \Delta_{ab}^{\text{prox}} \leq \epsilon\}$.

*Core Object*. A point $a$ is specified as a core object if its $\epsilon$-neighborhood consists of a minimum number of neighbors, $N_{\min}$, i.e., $|\mathcal{N}_a^{\epsilon}| \geq N_{\min}$. A point $b$ is considered directly density-reachable (DDR) from a core object $a$ if, $b \in \mathcal{N}_a^{\epsilon}$. If there are multiple points between $b$ and $a$, DDR from each other consecutively, then $b$ is considered density-reachable (DR) from $a$. A core object $b$ is considered density-connected (DC) to a core object $a$ if a common point, $c$, is DR from both, i.e., $c \in \mathcal{N}_a^{\epsilon}$ and $c \in \mathcal{N}_b^{\epsilon}$. A point $b$ is considered as a border point if it is not a core object but it is DR from another core object.

*Density Based Cluster*. A density based cluster consists of points that are DR or DC to each other, w.r.t. $\epsilon$ and $N_{\min}$.

We can see from above that $\epsilon$ and $N_{\min}$ are the two most important parameters for DBSCAN. The algorithm essentially searches for core objects based on these parameters and then extends the clusters through DR and/or DC relations. It is also clear that clusters can take arbitrary shapes. Points which are not part of the clusters are considered as noise. We refer the reader to [53] for further details on implementation of DBSCAN.

### *B. Focusing with Extended DBSCAN*

The most challenging scenario for DBSCAN is the scenario when two or more clusters are in close proximity to each other. Despite fine-tuning $\epsilon$ and $N_{\min}$, there is a chance that multiple clusters in close proximity might merge into each other. In our case, the primary aim of FS-SAR mode is to enhance the AR. This is particularly important when the targets are in close proximity to each other. Thus, a straightforward application of DBSCAN may impact AR enhancement negatively. To prevent this, like [52], we introduce a non-spatial parameter, $\rho$, for DBSCAN, along with $\epsilon$ and $N_{\min}$. We call it extended DBSCAN (EDBSCAN). The parameter $\rho$ relates to the intensities of the points. The Euclidean distance between the intensities of two points, $a$ at $(x_i, y_j)$ and $b$ at $(x_{i'}, y_{j'})$, can be written as, $\Delta_{ab}^{\text{intens}} = \sqrt{(\gamma_{ij} - \gamma_{i'j'})^2}$, where $\gamma_{ij}$ and $\gamma_{i'j'}$ are the intensities of the points $a$ and $b$, respectively. Note, the introduction of $\rho$ follows the same philosophy of fusion as in (12) or (15), i.e., an extended object has smoother transitions in its reflectivities and different objects will have abrupt discontinuities between their reflectivities. In EDBSCAN, the neighborhood is dependent on both $\epsilon$ and $\rho$. Thus, the $\epsilon\rho$-neighborhood of the point $a$ can be defined as, $\mathcal{N}_a^{\epsilon\rho} \triangleq \{b \in \mathcal{P} : \Delta_{ab}^{\text{prox}} \leq \epsilon, \Delta_{ab}^{\text{intens}} \leq \rho\}$. A point $a$ is considered as a core object if its $\epsilon\rho$-neighborhood consists of a minimum number of neighbors, $N_{\min}$, i.e., $|\mathcal{N}_a^{\epsilon\rho}| \geq N_{\min}$. The relations, i.e., DDR, DR and DC in DBSCAN are extended to EDBSCAN, in a similar way, to generate the clusters.

Once the dynamic part of the measurements has been obtained (see Section III-B), we apply EDBSCAN on the composite image i.e., $\gamma^{\hat{\mathbf{S}}}$, instead of aperture-wise image, i.e., $\gamma^{\hat{\mathbf{s}}_l}$. The reason is that a composite image contains more information regarding the target and its trajectory. Segmentation via EDBSCAN creates a cluster of a moving target along with its trajectory. We can see that EDBSCAN is especially useful in automotive scenarios where multiple moving targets can acquire any trajectory. Therefore, the segmentation procedure should be able to handle clusters of arbitrary shapes as well as being able to resolve clusters in close proximity.

Now, in order to focus the image, we intersect individual clusters with aperture-wise images. This generates the contributions of each aperture to the cluster. The image can now be focused on the last aperture image (or any other aperture image, if required) via correlation maximisation. After image focusing, the dynamic-part image can be combined with the clutter-part image to generate a final focused image of the target scene.

## V. Proposed Method Implementation

In this section, we provide step-by-step details on implementing the proposed method.

1) Measurements are obtained according to (9). Here, we assume that the measurements correspond to a specific target area and that the radar motion has been compensated w.r.t. the stationary objects. Thus, the only movement noticeable in the measurements is due to the moving targets. The measurements are stacked together, according to (14) to obtain $\mathbf{Y}$.
2) We use ADMM to estimate $\mathbf{X}$ as an inverse problem for FS-SAR mode, along with decomposing it into a clutter matrix $\mathbf{C}$ and a sparse matrix $\mathbf{S}$ via LPSD in (15). To this end, we iterate over (18)–(25). We consider a warm-start for the estimate of $\mathbf{X}$, i.e., $\hat{\mathbf{X}}^{[0]} = \mathbf{\Phi}^H \mathbf{Y}$, which is akin to matched filtering. We initialise $\mathbf{C}$, $\mathbf{S}$, $\mathbf{Z}$, $\mathbf{W}$, $\mathbf{K}_X$, $\mathbf{K}_Z$ and $\mathbf{K}_W$ as null matrices. Our stopping criterion for iterations is both the maximum number of iterations as well as the update tolerance of $\hat{\mathbf{X}}^{[n]}$. The final estimates correspond to the values when iterations have stopped.
3) The estimates $\hat{\mathbf{X}}$, $\hat{\mathbf{C}}$ and $\hat{\mathbf{S}}$ can be used to form the respective images. For this, we use back-projection as in [15]. Mathematically, the image formation can be represented as follows. A composite image of all the aperture samples at point $(x_i, y_j)$ can be written as

$$\gamma_{ij}^{\hat{\mathbf{X}}} = \sum_{l=0}^{L-1} [\uparrow_{1,\kappa'} (\hat{\mathbf{X}}_l)]_{I_{\theta_{ij}}, I_{r_{ij}}} \tag{33}$$

where $\uparrow_{\kappa,\kappa'} (\cdot)$ denotes an upsampling function which interpolates a matrix by an order $\kappa$ along its rows and by an order $\kappa'$ along its columns, $\hat{\mathbf{X}}_l$ is the reshaped

matrix form of $\hat{\mathbf{x}}_l$ (see (11)), $I_{\theta_{ij}}$ is the row index and $I_{r_{ij}}$ is the column index in $\uparrow_{1,\kappa'}(\hat{\mathbf{X}}_l)$, corresponding to angle $\theta_{ij}$ and range $r_{ij}$, respectively. The composite image can be related to aperture-wise images as

$$\gamma^{\hat{\mathbf{X}}} = \sum_{l=0}^{L-1} \gamma^{\hat{\mathbf{x}}_l} \tag{34}$$

where $\gamma^{\hat{\mathbf{x}}_l}$ is essentially the back-projected image of $\hat{\mathbf{x}}_l$, with $\hat{\mathbf{x}}_l$ being first reshaped into $\hat{\mathbf{X}}_l$. Similarly, composite images, i.e., $\gamma^{\hat{\mathbf{C}}}$ and $\gamma^{\hat{\mathbf{S}}}$, and aperture-wise images, i.e., $\gamma^{\hat{\mathbf{c}}_l}$ and $\gamma^{\hat{\mathbf{s}}_l}$, w.r.t. $\hat{\mathbf{C}}$ and $\hat{\mathbf{S}}$ can be obtained accordingly.

4) We apply EDBSCAN on the composite dynamic image $\gamma^{\hat{\mathbf{S}}}$. Since $\hat{\mathbf{S}}$ is sparse, $\gamma^{\hat{\mathbf{S}}}$ is also sparse, containing few objects represented by a continuum of reflective points. We tune parameters $\epsilon$, $\rho$ and $N_{\min}$. We select $\epsilon$ as a function of image spatial resolution, $\rho$ as a function of pixel intensities and $N_{\min}$ as a function of $\epsilon$.
5) The composite dynamic image can be represented as a sum of clusters, i.e.,

$$\gamma^{\hat{\mathbf{S}}} = \sum_{u=0}^{\breve{U}-1} \gamma^{\hat{\mathbf{S}}}[\mathcal{U}_u] \tag{35}$$

where $\gamma^{\hat{\mathbf{S}}}[\mathcal{U}_u]$ represent the image ($\gamma^{\hat{\mathbf{S}}}$) with only $u$th cluster present. Now, for image focusing, we intersect each cluster image with aperture-wise images, i.e.,

$$\gamma^{\hat{\mathbf{s}}_l}_{i:j:}[\mathcal{U}_u] = \gamma^{\hat{\mathbf{s}}_l} \bigcap \gamma^{\hat{\mathbf{S}}}[\mathcal{U}_u] \tag{36}$$

where $\gamma^{\hat{\mathbf{s}}_l}_{i:j:}[\mathcal{U}_u]$ represents an image patch with the contribution of $l$th aperture in $u$th cluster and $i{:}j{:}$ represents a range of $i$ and $j$ values. Let the image is focused on the last aperture position and $\gamma^{\hat{\mathbf{s}}_{L-1}}[\mathcal{U}_u]$ represents the image with only the contribution of $L-1$th aperture for $u$th cluster. Then, the focused image for $u$th target can be obtained as

$$\tilde{\gamma}^{\hat{\mathbf{S}}}[u] = \sum_{l=0}^{L-2} \text{align}\left(\gamma^{\hat{\mathbf{s}}_l}_{i:j:}[\mathcal{U}_u], \gamma^{\hat{\mathbf{s}}_{L-1}}[\mathcal{U}_u]\right) \tag{37}$$

where the $\text{align}(\cdot,\cdot)$ function merges two images based on 2-D cross-correlation maximisation. A focused image of all the moving targets can be obtained as

$$\tilde{\gamma}^{\hat{\mathbf{S}}} = \sum_{u=0}^{\breve{U}-1} \tilde{\gamma}^{\hat{\mathbf{S}}}[u] \tag{38}$$

and the final focused image including the clutter and dynamic targets can be obtained as

$$\tilde{\gamma}^{\hat{\mathbf{X}}} = \tilde{\gamma}^{\hat{\mathbf{S}}} + \gamma^{\hat{\mathbf{C}}}. \tag{39}$$

## VI. Experimental Verification

In this section, we provide experimental results to verify our proposed methodology. We present both simulation as well as real-data experiments for this purpose. We use MBP to show the measured signal. MBP in [15] is defined as

$$\gamma_{ij} = \sum_{\theta} \sum_{l} [\uparrow_{\kappa,\kappa} (\mathbf{Y}_l)]_{\theta, I_{r_{ij}}}. \tag{40}$$

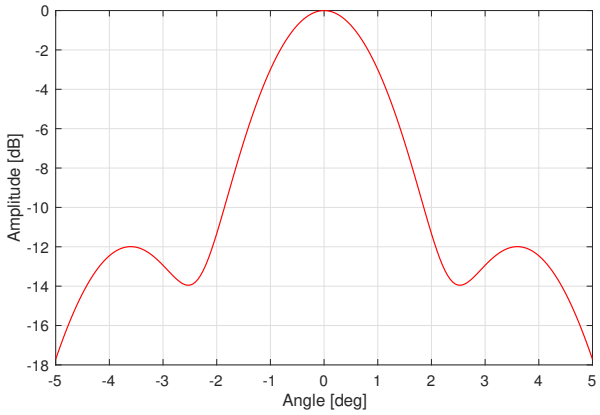


Fig. 2: Antenna Pattern [15].

We compare the performance of our proposed algorithm with CBP. Note, CBP essentially consists of using the solution of (12) in (33).

### A. Simulation

We consider an FMCW radar operating at $f_0 = 300$ GHz. With a signal bandwidth $B = 6$ GHz, the range resolution can be calculated as, $\Delta_r = 0.025$ m. As in [15], we consider $\theta_{3\text{dB}} \approx 2^\circ$ and deterministically emulate the beam-pattern as suggested by [61]. Figure 2 shows the beam-pattern. The target scene is considered as a 2-D grid of spatial resolution $\Delta_r$. Figure 3 shows the target scene. There are 8 extended targets in total, of size $5\times4$ grid cells. There are 6 stationary targets to represent the clutter and 2 moving targets. The moving targets move along $x$-axis in opposite directions. At each aperture step, moving targets travel 4 grid cells along $x$-axis. Since the radar motion has already been compensated, we assume the radar is referenced at $(x_0, y_0)$. We consider $L = 20$ aperture frames, with scan angle range $\theta_{\min} = -20^\circ$ and $\theta_{\max} = +20^\circ$, at angular intervals $\Delta_\theta = 0.25^\circ$.

Figures 3a–3d show target scene at aperture frames $l = 0$, $l = 7$, $l = 15$ and $l = 19$, respectively. We can see that at each aperture position, the reflectivity of clutter targets varies. Thus, the clutter targets are not strictly fixed. However, the moving targets have fixed reflectivity. Figure 4a shows the result of image reconstruction via MBP. We can see that due to the movement of targets, reconstructed image is smeared. Now, in order to compare the performance of our proposed algorithm, we also present the results of applying CBP. Figure 4b shows the performance of image reconstruction via CBP. Since CBP does not consider the movement of the targets, the reconstructed image is smeared over the trajectories of the moving targets. However, we can see an improvement in AR, as the gap is evident between the trajectories of the targets. Figure 5 shows the performance results of applying our proposed matrix decomposition approach. We can see from Figures 5a and 5b that the clutter/stationary targets have been completely separated from the dynamic/moving targets. Figure 5c shows the combined result of clutter targets and the dynamic targets. We can see that due to our proposed OP,

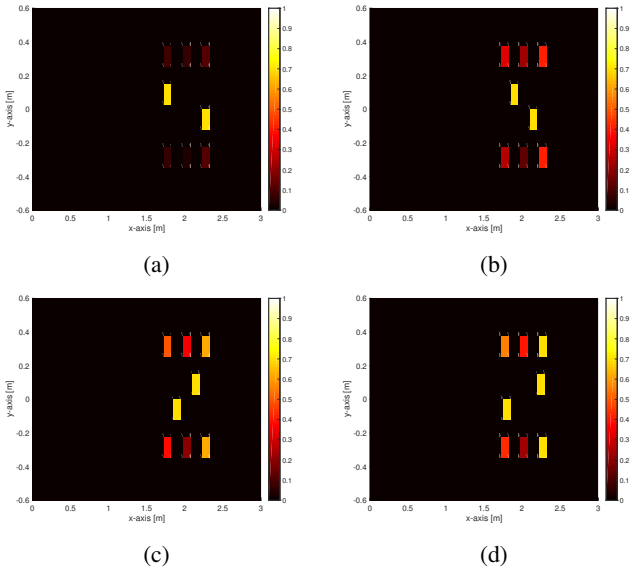


(a) (b) (c) (d)

Fig. 3: Target scene, aperture step: (a) $l = 0$, (b) $l = 7$, (c) $l = 15$, (d) $l = 19$.

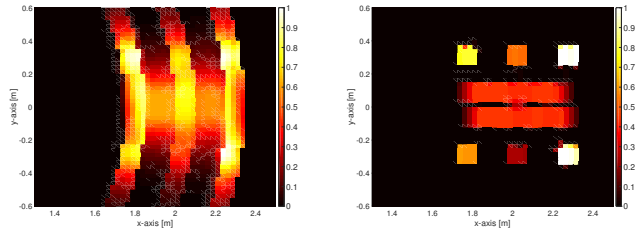


(a) (b)

Fig. 4: Reconstructed image via: (a) MBP (b) CBP.

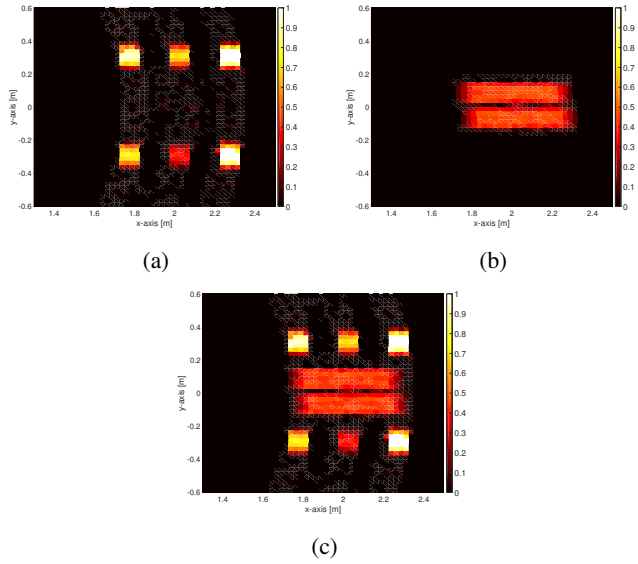


(a) (b) (c)

Fig. 5: Composite image: (a) clutter only, $\gamma^{\hat{\mathbf{C}}}$ (b) dynamic-part only, $\gamma^{\hat{\mathbf{S}}}$ (c) combined, $\gamma^{\hat{\mathbf{X}}}$.

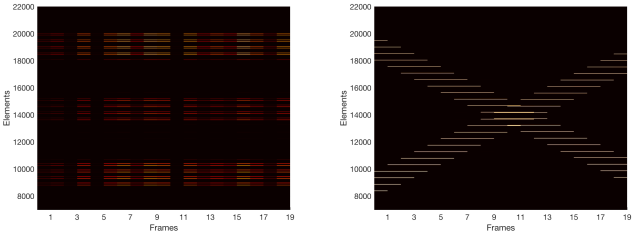


(a) (b)

Fig. 6: Matrices: (a) $\hat{\mathbf{C}}$ (b) $\hat{\mathbf{S}}$

we obtain good AR enhancement like CBP. However, in the proposed formulation, we are also able to separate the dynamic part from the clutter. In Figure 6a and 6b, we plot matrices $\hat{\mathbf{C}}$ and $\hat{\mathbf{S}}$, in order to get an insight into LPSD. We can see that frames (i.e., columns of the matrix) in $\hat{\mathbf{C}}$ are correlated with each other whereas the frames in $\hat{\mathbf{S}}$ are uncorrelated and dynamic. Thus, LPSD for FS-SAR is a viable non-parametric option to separate clutter from the moving targets.

Nonetheless, we can see from Figure 5b that the image of the moving targets is still smeared (along the direction of motion) and it needs to be focused. To this end, we use EDBSCAN. We consider EDBSCAN parameters as, $N_{\min} = 10$, $\epsilon = 0.05$ m and $\rho = 0.12$. Figure 7a shows the result of applying EDBSCAN. We can see that the two targets along with their respective trajectories form two clusters. Despite their proximity, EDBSCAN has been able to separate the two clusters and provide good segmentation results. Then, we focus the image as explained in step 5) of Section V. Figure 7b shows the result of focusing. We can see that the targets are well focused on the last aperture step. Figure 7c shows the combined image of clutter and dynamic targets with focusing. We can see that the final reconstructed image shows improved AR as well a good focusing of the moving targets.

Note, the above results show the performance of our proposed method in the absence of measurement noise. However, it can be shown that a good performance can be achieved in the presence of noise as well. Figure 8 shows the performance of the proposed method for a signal-to-noise ratio (SNR) of 10 dB, where the SNR is defined in terms of (14) as

$$\text{SNR} \triangleq \frac{\|\mathbf{\Phi X}\|_F^2}{N_\theta N_r \nu^2}. \tag{41}$$

Comparing Figures 5 and 7c with Figure 8, we can see that the proposed method provides a good performance even in the presence of noise. Note, here we consider EDBSCAN parameters as, $N_{\min} = 10$, $\epsilon = 0.05$ m and $\rho = 0.14$.

TABLE I: Specifications of 300 GHz Radar

| | |
|---|---|
| Modulation | FMCW |
| Frequency Range | $287 - 293$ GHz |
| Transmit Bandwidh ($B$) | 6 GHz |
| Chirp Duration ($T$) | 1 ms |
| Sampling Frequency | 4.096 MHz |
| Angular Step ($\Delta_\theta$) | $0.25^\circ$ |
| Range Resolution ($\Delta_r$) | 0.025 m |
| 3 dB Beamwidth ($\theta_{3\text{dB}}$) | $1.3^\circ$ |

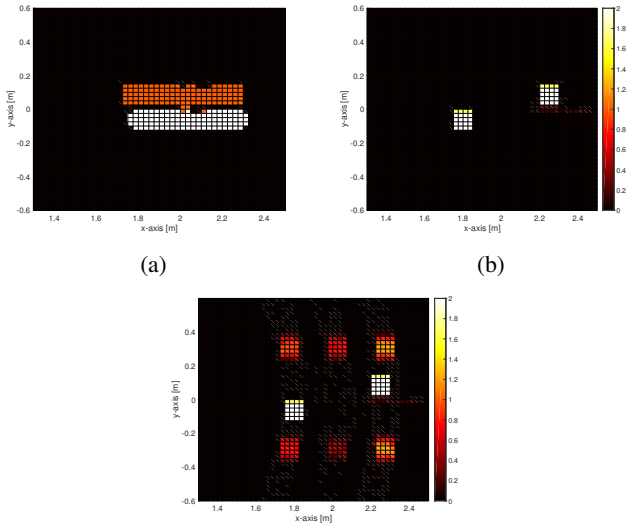


Fig. 7: (a) Clustering via EDBSCAN (b) Focused image, $\tilde{\gamma}^{\hat{\mathbf{S}}}$ (c) Focused image, $\tilde{\gamma}^{\hat{\mathbf{X}}}$.

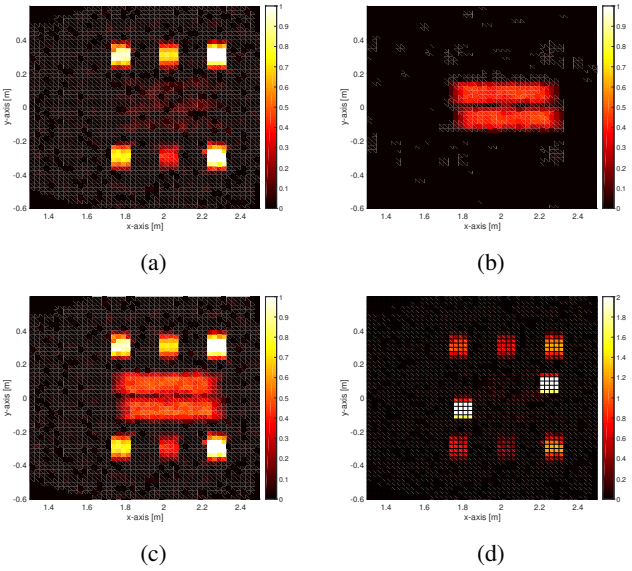


Fig. 8: Imaging in the presence of noise: (a) clutter only, $\gamma^{\hat{\mathbf{C}}}$ (b) dynamic-part only, $\gamma^{\hat{\mathbf{S}}}$ (c) combined image, $\gamma^{\hat{\mathbf{X}}}$ (d) focused image, $\tilde{\gamma}^{\hat{\mathbf{X}}}$.

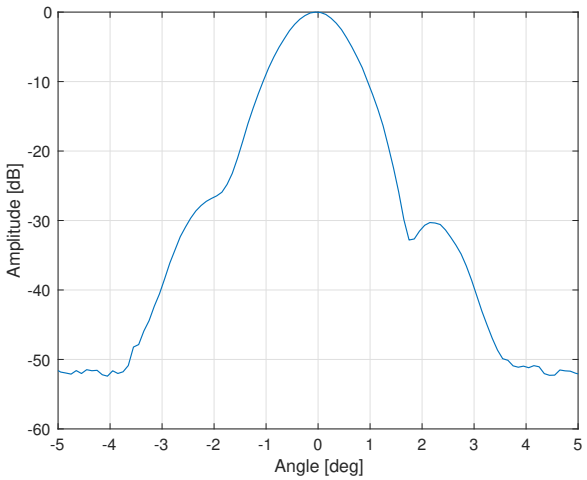


Fig. 9: Measured Antenna Pattern for 300 GHz radar.

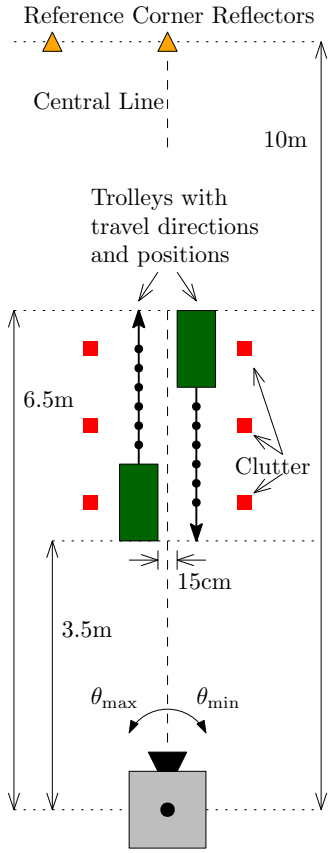


Fig. 10: Measurements schematic.

### *B. Real Data*

In order to carry out real-data experiments (in controlled laboratory conditions), we have considered a $f_0 = 300$ GHz FMCW radar with transmit bandwidth $B = 6$ GHz. Figure 9 shows the measured antenna pattern with 3 dB beamwidth $\theta_{3\text{dB}} \approx 1.3°$. Table I shows the specifications of the radar. Figure 10 shows the schematic for the measurement setup. We consider 2 trolleys of size $1 \times 0.5 \times 0.55$ (length $\times$ width $\times$ height) m$^3$, as our extended moving targets. We consider 6 traffic cones as stationary targets, i.e., scene clutter. We consider $L = 21$ aperture steps/frames, with scan angle range $\theta_{\min} = -20°$ and $\theta_{\max} = +20°$, at angular intervals $\Delta_\theta = 0.25°$. At each aperture step, the trolleys move by 10 cm in opposite direction along the $x$-axis. Figure 11 shows the 300 GHz radar used for the measurements. Figure 12 shows the target scene at different aperture positions, i.e., $l = 0$, $l = 10$ and $l = 20$. The EDBSCAN parameters are considered as, $N_{\min} = 12$, $\epsilon = 0.1$ m and $\rho = 0.1$.

Figure 13a shows the measured scene by reconstructing the

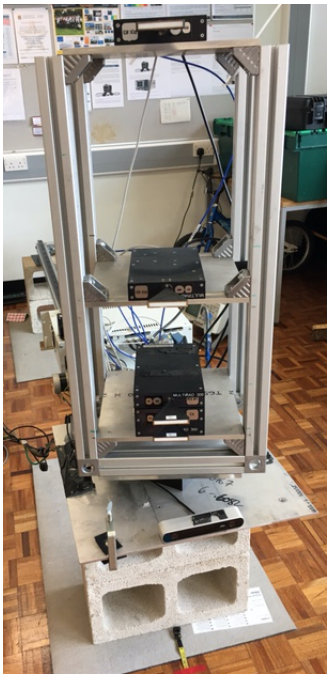

Fig. 11: 300 GHz radar.

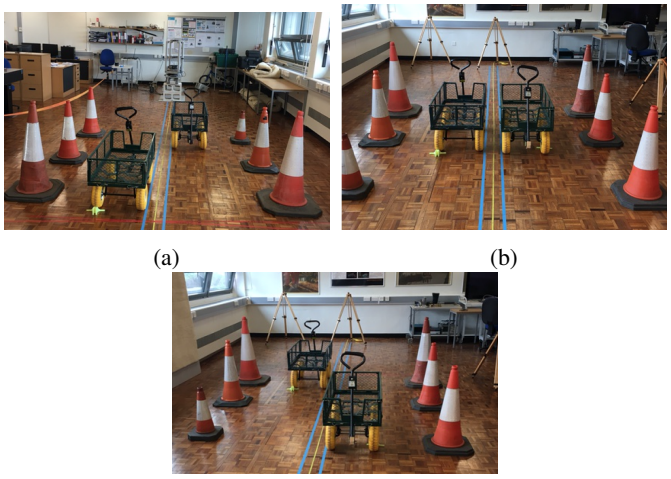

(a) (b)

(c)

Fig. 12: Moving targets and clutter: (a) $l = 0$ (b) $l = 10$ (c) $l = 20$

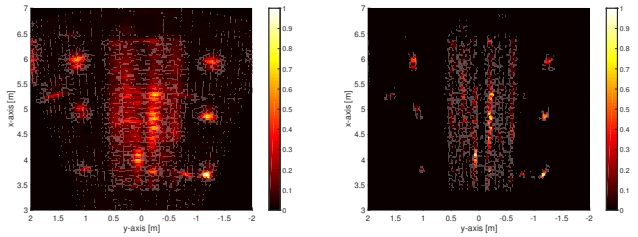

(a) (b)

Fig. 13: Reconstructed image via: (a) MBP (b) CBP.

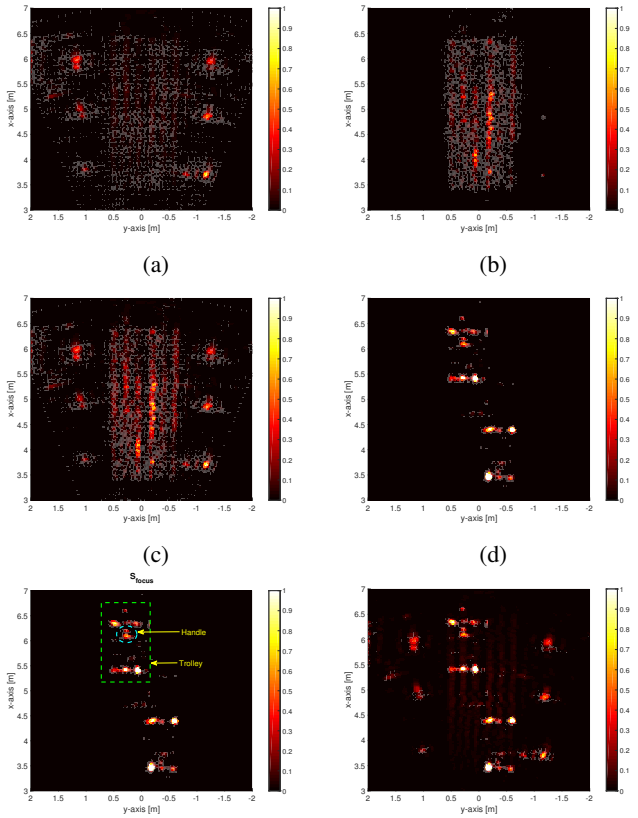


(a) (b)

(c) (d)

(e) (f)

Fig. 14: Composite image: (a) clutter only, $\gamma^{\hat{\mathbf{C}}}$ (b) dynamic-part only, $\gamma^{\hat{\mathbf{S}}}$ (c) combined, $\gamma^{\hat{\mathbf{X}}}$ (d) focused, dynamic-part only, $\tilde{\gamma}^{\hat{\mathbf{S}}}$ (e) $\tilde{\gamma}^{\hat{\mathbf{S}}}$ with labels (f) focused, combined, $\tilde{\gamma}^{\hat{\mathbf{X}}}$.

image via MBP. As expected, image of the moving targets is smeared. Although, some improvement in the AR is visible. Figure 13b shows the reconstructed image via CBP. We can see that the AR is better than the MBP. However, the patch for the moving targets is still smeared because, like MBP, CBP also does not consider target movement. Note, the maximum intensity value of the images has been normalised to unity, in this section. Figure 14 shows the result of applying our proposed method. Figures 14a–14c show the performance of our proposed image decomposition approach for clutter only, dynamic-part only and their combination, respectively. We can see from Figures 14a and 14b that the clutter has been successfully separated from the dynamic part. Figure 14d shows the performance of our image focusing method on the dynamic-part only image. In comparison to Figure 14b, we can see that the image of the moving targets is well-focused. Even the details of the trolley, e.g., handle, are also visible (see Figure 14e with labels). Figure 14f shows the combined focused image of the clutter and the moving targets. We can see that our proposed method has achieved substantially improved AR as well as image focusing for both the clutter and the moving targets.

## VII. Conclusions

In this paper, we have extended the FS-SAR methodology to imaging moving targets in automotive scenarios. We have adapted a non-parametric matrix decomposition approach to

FS-SAR in order to separate the dynamic part of the image from the clutter. In the process, we have also obtained trajectories of the moving targets. We have proposed an ADMM based iterative method to solve our optimisation problem. To focus the image, i.e., to build the synthetic aperture, we have proposed an extended DBSCAN method to achieve spatial segmentation along with the application of cross-correlation maximisation. We have achieved well-focused imaging of the moving targets along with improved angular resolution. We have provided experimental results, both with simulation as well as real-data, to prove the validity of our proposed method.

## ACKNOWLEDGEMENTS

This work has been approved by TASSC-PATHCAD sponsor, Chris Holmes, Senior Manager Research, Research Department, Jaguar Land Rover, Coventry, UK.
All real-data supporting this work are openly available from The University of Edinburgh repository (DataShare) at https://doi.org/10.7488/ds/2586.

## REFERENCES

[1] K. Bengler, K. Dietmayer, B. Farber, M. Maurer, C. Stiller, and H. Winner, "Three decades of driver assistance systems: Review and future perspectives," *IEEE Intelligent Transportation Systems Magazine*, vol. 6, no. 4, pp. 6–22, winter 2014.

[2] A. Eskandarian, *Handbook of Intelligent Vehicles*. NY, USA: Springer-Verlag, 2012.

[3] E. Guizzo, "How Google's self-driving car works," *IEEE Spectrum Online*, Oct. 2011.

[4] S. Palm, R. Sommer, M. Caris, N. Pohl, A. Tessmann, and U. Stilla, "Ultra-high resolution SAR in lower terahertz domain for applications in mobile mapping," in *2016 GeMiC*, March 2016, pp. 205–208.

[5] D. Jasteh, E. G. Hoare, M. Cherniakov, and M. Gashinova, "Experimental low-terahertz radar image analysis for automotive terrain sensing," *IEEE Geoscience and Remote Sensing Letters*, vol. 13, no. 4, pp. 490–494, April 2016.

[6] M. Murad, I. Bilik, M. Friesen, J. Nickolaou, J. Salinger, K. Geary, and J. S. Colburn, "Requirements for next generation automotive radars," in *IEEE Radar Conference (RadarCon13)*, April 2013, pp. 1–6.

[7] S. M. Patole, M. Torlak, D. Wang, and M. Ali, "Automotive radars: A review of signal processing techniques," *IEEE Signal Processing Magazine*, vol. 34, no. 2, pp. 22–35, March 2017.

[8] G. Krieger, J. Mittermayer, S. Buckreuss, M. Wendler, T. Sutor, F. Witte, and A. Moreira, "Sector imaging radar for enhanced vision," *Aerospace Science and Technology*, vol. 7, no. 2, pp. 147 – 158, 2003.

[9] A. Farina, F. Gini, and M. Greco, "DOA estimation by exploiting the amplitude modulation induced by antenna scanning," *IEEE Transactions on Aerospace and Electronic Systems*, vol. 38, no. 4, pp. 1276–1286, Oct 2002.

[10] G. Liu, K. Yang, B. Sykora, and I. Salha, "Range and azimuth resolution enhancement for 94 GHz real-beam radar," in *Proceedings of SPIE on Radar Sensor Technology XII*, vol. 6947, 2008, pp. 1–9.

[11] S. Uttam and N. A. Goodman, "Superresolution of coherent sources in real-beam data," *IEEE Transactions on Aerospace and Electronic Systems*, vol. 46, no. 3, pp. 1557–1566, July 2010.

[12] M. A. Richards, "Iterative noncoherent angular superresolution [radar]," in *Proceedings of the IEEE National Radar Conference*, Apr 1988, pp. 100–105.

[13] M. Ruggiano, E. Stolp, and P. van Genderen, "Improvement of target resolution in azimuth by lmmse technique," in *European Radar Conference (EuRAD)*, Sept 2009, pp. 230–233.

[14] J. Guan, J. Yang, Y. Huang, and W. Li, "Maximum a posteriori based angular superresolution for scanning radar imaging," *IEEE Transactions on Aerospace and Electronic Systems*, vol. 50, no. 3, pp. 2389–2398, July 2014.

[15] S. Gishkori, L. Daniel, M. Gashinova, and B. Mulgrew, "Imaging for a forward scanning automotive synthetic aperture radar," *IEEE Transactions on Aerospace and Electronic Systems*, p. to appear, 2018.

[16] M. Soumekh, *Synthetic Aperture Radar Signal Processing with MATLAB Algorithms*. NY, USA: John Wiley & Sons, Inc., 1999.

[17] D. L. Donoho, "Compressed sensing," *IEEE Transactions on Information Theory*, vol. 52, no. 4, April 2006.

[18] E. Candes, J. Romberg, and T. Tao, "Robust uncertainty principles: exact signal reconstruction from highly incomplete frequency information," *IEEE Transactions on Information Theory*, vol. 52, no. 2, pp. 489–509, Feb. 2006.

[19] R. K. Raney, "Synthetic aperture imaging radar and moving targets," *IEEE Transactions on Aerospace and Electronic Systems*, vol. AES-7, no. 3, pp. 499–505, May 1971.

[20] S. Barbarossa and A. Farina, "Space-time-frequency processing of synthetic aperture radar signals," *IEEE Transactions on Aerospace and Electronic Systems*, vol. 30, no. 2, pp. 341–358, April 1994.

[21] M. Soumekh, *Fourier Array Imaging*. Englewood Cliffs, NJ, USA: Prentice-Hall, 1994.

[22] C. V. Jakowatz, D. E. Wahl, and P. H. Eichel, "Refocus of constant-velocity moving targets in synthetic aperture radar imagery," *Proc. SPIE*, vol. 3370, pp. 85–95, 1998.

[23] J. K. Jao, "Theory of synthetic aperture radar imaging of a moving target," *IEEE Transactions on Geoscience and Remote Sensing*, vol. 39, no. 9, pp. 1984–1992, Sep. 2001.

[24] A. Yegulalp, "Analysis of sar image formation equations for stationary and moving targets," MIT Lincoln Laboratory, Tech. Rep., Jun. 2002.

[25] M. I. Pettersson, "Detection of moving targets in wideband SAR," *IEEE Transactions on Aerospace and Electronic Systems*, vol. 40, no. 3, pp. 780–796, July 2004.

[26] V. T. Vu, T. K. Sjogren, M. I. Pettersson, A. Gustavsson, and L. M. H. Ulander, "Detection of moving targets by focusing in UWB SAR: Theory and experimental results," *IEEE Transactions on Geoscience and Remote Sensing*, vol. 48, no. 10, pp. 3799–3815, Oct. 2010.

[27] J. R. Fienup, "Detecting moving targets in SAR imagery by focusing," *IEEE Transactions on Aerospace and Electronic Systems*, vol. 37, no. 3, pp. 794–809, Jul. 2001.

[28] P. A. C. Marques and J. M. B. Dias, "Moving targets processing in SAR spatial domain," *IEEE Transactions on Aerospace and Electronic Systems*, vol. 43, no. 3, pp. 864–874, July 2007.

[29] T. K. Sjogren, V. T. Vu, M. I. Pettersson, A. Gustavsson, and L. M. H. Ulander, "Moving target relative speed estimation and refocusing in synthetic aperture radar images," *IEEE Transactions on Aerospace and Electronic Systems*, vol. 48, no. 3, pp. 2426–2436, JULY 2012.

[30] B. Friedlander and B. Porat, "VSAR: a high resolution radar system for detection of moving targets," *IEE Proceedings - Radar, Sonar and Navigation*, vol. 144, no. 4, pp. 205–218, Aug 1997.

[31] M. A. Sletten, L. Rosenberg, S. Menk, J. V. Toporkov, and R. W. Jansen, "Maritime signature correction with the NRL multichannel SAR," *IEEE Transactions on Geoscience and Remote Sensing*, vol. 54, no. 11, pp. 6783–6790, Nov 2016.

[32] J. Ward, "Space-time adaptive processing for airborne radar," in *IEE Colloquium on Space-Time Adaptive Processing (Ref. No. 1998/241)*, April 1998, pp. 2/1–2/6.

[33] J. H. G. Ender, "Space-time processing for multichannel synthetic aperture radar," *Electronics Communication Engineering Journal*, vol. 11, no. 1, pp. 29–38, Feb 1999.

[34] A. Farina and P. Lombardo, "Space-time techniques for SAR," in *Applications of Space-Time Adaptive Processing*, ser. 14, R. Klemm, Ed. London, UK: IET, 2004, ch. 3, pp. 73–122.

[35] D. Cerutti-Maori, C. H. Gierull, and J. H. G. Ender, "Experimental verification of SAR-GMTI improvement through antenna switching," *IEEE Transactions on Geoscience and Remote Sensing*, vol. 48, no. 4, pp. 2066–2075, Apr. 2010.

[36] S. Zhu, G. Liao, Z. Zhou, and Y. Qu, "Robust moving targets detection and velocity estimation using multi-channel and multi-look SAR images," *Signal Process.*, vol. 90, no. 6, pp. 2009–2019, jun. 2010.

[37] J. Xu, Y. Zuo, B. Xia, X. Xia, Y. Peng, and Y. Wang, "Ground moving target signal analysis in complex image domain for multichannel SAR," *IEEE Transactions on Geoscience and Remote Sensing*, vol. 50, no. 2, pp. 538–552, Feb 2012.

[38] N. Onhon and M. Cetin, "SAR moving target imaging in a sparsity-driven framework," in *Proc. SPIE on Wavelets and Sparsity XIV*, vol. 8138, 2011.

[39] M. Yasin, M. Cetin, and A. S. Khwaja, "SAR imaging of moving targets by subaperture based low-rank and sparse decomposition," in *25th Signal Processing and Communications Applications Conference (SIU)*, May 2017, pp. 1–4.

[40] A. Soganli and M. Cetin, "Low-rank sparse matrix decomposition for sparsity-driven SAR image reconstruction," in *International Workshop on Compressed Sensing Theory and its Applications to Radar, Sonar and Remote Sensing (CoSeRa)*, Jun. 2015, pp. 239–243.

[41] E. Candes and B. Recht, "Exact matrix completion via convex optimization," *Foundations of Computational Mathematics*, vol. 9, no. 6, pp. 717–772, Apr. 2009.

[42] J.-F. Cai, E. Candes, and Z. Shen, "A singular value thresholding algorithm for matrix completion," *SIAM J. on Optimization*, vol. 20, no. 4, pp. 1956–1982, Mar. 2010.

[43] V. Chandrasekaran, S. Sanghavi, P. Parrilo, and A. Willsky, "Rank-sparsity incoherence for matrix decomposition," *SIAM Journal on Optimization*, vol. 21, no. 2, pp. 572–596, 2011.

[44] E. Candes, X. Li, Y. Ma, and J. Wright, "Robust principal component analysis?" *J. ACM*, vol. 58, no. 3, pp. 1–37, Jun. 2011.

[45] S. Lingala, Y. Hu, E. DiBella, and M. Jacob, "Accelerated dynamic MRI exploiting sparsity and low-rank structure: k-t SLR," *IEEE Transactions on Medical Imaging*, vol. 30, no. 5, pp. 1042–1054, May 2011.

[46] X. Zhou, C. Yang, and W. Yu, "Moving object detection by detecting contiguous outliers in the low-rank representation," *IEEE Transactions on Pattern Analysis and Machine Intelligence*, vol. 35, no. 3, pp. 597–610, Mar. 2013.

[47] R. Otazo, E. Candes, and D. Sodickson, "Low-rank plus sparse matrix decomposition for accelerated dynamic MRI with separation of background and dynamic components," *Magnetic Resonance in Medicine*, vol. 73, no. 3, pp. 1125–1136, Mar. 2015.

[48] S. Boyd, N. Parikh, E. Chu, B. Peleato, and J. Eckstein, "Distributed optimization and statistical learning via the alternating direction method of multipliers," *Found. Trends Mach. Learn.*, vol. 3, no. 1, pp. 1–122, Jan. 2011.

[49] D. P. Bertsekas and J. N. Tsitsiklis. Parallel and Distributed Computation: Numerical Methods, 1997.

[50] C. M. Bishop, *Pattern Recognition and Machine Learning (Information Science and Statistics)*. Berlin, Heidelberg: Springer-Verlag, 2006.

[51] M. Ester, H.-P. Kriegel, J. Sander, and X. Xu, "A density-based algorithm for discovering clusters a density-based algorithm for discovering clusters in large spatial databases with noise," in *Proceedings of the Second International Conference on Knowledge Discovery and Data Mining*, 1996, pp. 226–231.

[52] D. Birant and A. Kut, "ST-DBSCAN: An algorithm for clustering spatial-temporal data," *Data Knowl. Eng.*, vol. 60, no. 1, pp. 208–221, Jan. 2007.

[53] E. Schubert, J. Sander, M. Ester, H. P. Kriegel, and X. Xu, "DBSCAN revisited, revisited: Why and how you should (still) use DBSCAN," *ACM Trans. Database Syst.*, vol. 42, no. 3, pp. 1–21, Jul. 2017.

[54] W. Carrara, R. Goodman, and R. Majewski, *Spotlight Synthetic Aperture Radar*. Boston: Artech House, 1995.

[55] M. A. Richards, *Fundamentals of Radar Signal Processing*. Two Penn Plaza, NY, USA: McGraw-Hill Companies, Inc., 2005.

[56] A. Meta, P. Hoogeboom, and L. P. Ligthart, "Signal processing for FMCW SAR," *IEEE Transactions on Geoscience and Remote Sensing*, vol. 45, no. 11, pp. 3519–3532, Nov 2007.

[57] A. Ribalta, "Time-domain reconstruction algorithms for FMCW-SAR," *IEEE Geoscience and Remote Sensing Letters*, vol. 8, no. 3, pp. 396–400, May 2011.

[58] M. Grant and S. Boyd, "CVX: Matlab software for disciplined convex programming," Mar. 2014.

[59] X. Yuan and J. Yang, "Sparse and low rank matrix decomposition via alternating direction method," vol. 9, pp. 167–180, Jan. 2009.

[60] R. Tibshirani, M. Saunders, S. Rosset, J. Zhu, and K. Knight, "Sparsity and smoothness via the fused LASSO," *Journal of the Royal Statistical Society Series B*, pp. 91–108, 2005.

[61] M. Teichman, "Determination of horn antenna phase centers by edge diffraction theory," *IEEE Transactions on Aerospace and Electronic Systems*, vol. AES-9, no. 6, pp. 875–882, Nov 1973.


**Shahzad Gishkori** received the B.Sc. degree in electrical engineering from the University of Engineering and Technology Lahore, Lahore, Pakistan, in 2002, and the M.Sc. (cum Laude) and Ph.D. degrees both in electrical engineering from the Delft University of Technology, Delft, The Netherlands, in 2009 and 2014, respectively.

From 2014 to 2015, he was a Postdoctoral Research Associate with Imperial College London, London, U.K. Since February 2016, he has been working as a Postdoctoral Research Associate with the University of Edinburgh, Edinburgh, U.K. His research interests include compressed sensing, signal processing for wireless communications and image processing for automotive radars.

**David Wright** received a BSc. in Geophysics in 1998 from the University of Edinburgh, MSc. in applied Geophysics from the University of Durham in 1999 and PhD. in exploration Geophysics from the University of Edinburgh in 2004.

He was co-founder and senior geophysicist at MTEM Ltd. from 2004–2007 and senior research geophysicist at Petroleum Geo Services from 2007–2010. From 2010–2016 he was a research fellow in the School of Geosciences at the University of Edinburgh. Since January 2018 he has been a research associate at the institute of digital communications at the University of Edinburgh working on radar imaging for autonomous vehicles.

**Liam Daniel** received the M.Sc. degree in theoretical physics in 2005 and the Ph.D. degree in maritime forward scatter radar development in 2017, both from the University of Birmingham, Birmingham, U.K.

He is currently a Research Fellow at the Microwave Integrated Systems Laboratory, School of Engineering, University of Birmingham, Birmingham, U.K. His research interests include experimental, theoretical, simulation and signal processing aspects of bistatic radars with a focus on forward scatter radar and passive sensing, automotive sensing, and low-THz radar systems.

**Marina Gashinova** received the M.Math degree from St.-Petersburg State University, Saint Petersburg, Russia, in 1991, and the Ph.D. degree in physics and mathematics from St.-Petersburg Electrotechnical University, Saint Petersburg, Russia, in 2003.

In 2006, she joined the Microwave Integrated System Laboratory, University of Birmingham, Birmingham, U.K., as a Research Fellow. She is currently a Professor of Radar and RF Sensors, leading the research group on passive and active bistatic radar, THz multi-feature imaging radar, and automotive sensors.

**Bernard Mulgrew** (FIEEE, FREng, FRSE, FIET) received the B.Sc. degree from Queen's University Belfast, Belfast, U.K., in 1979, and the Ph.D. degree from University of Edinburgh, Edinburgh, U.K., in 1987.

After graduation, he worked for 4 years as a Development Engineer with the Radar Systems Department, Ferranti, Edinburgh. From 1983 to 1986, he was a Research Associate with the Department of Electrical Engineering, University of Edinburgh, Edinburgh, U.K. He was appointed as a Lecturer in 1986, promoted to a Senior Lecturer in 1994 and became a Reader in 1996. The University of Edinburgh appointed him to a Personal Chair in October 1999 (Professor of Signals and Systems). He has co-authored three books on signal processing. His research interests include adaptive signal processing and estimation theory and in their application to radar and sensor systems.